Available online at www.sciencedirect.com
SCIENCE DIRECT®
International Journal of Heat and Mass Transfer 49 (2006) 1703–1718
International Journal of HEAT and MASS TRANSFER
www.elsevier.com/locate/ijhmt

Nanoscale radiation heat transfer for silicon at different doping levels

C.J. Fu [a,b], Z.M. Zhang [a,*]

[a] George W. Woodruff School of Mechanical Engineering, Georgia Institute of Technology, Atlanta, GA 30332, USA
[b] Department of Mechanics and Engineering Science, Peking University, Beijing 100871, China

Received 26 April 2005; received in revised form 14 August 2005
Available online 20 December 2005

Abstract

Heat transfer between surfaces at close vicinity has important applications in nanoscale energy conversion devices and near-field scanning thermal microscopy. The present paper describes a comprehensive investigation of the radiation energy transfer between two semi-infinite parallel plates at different temperatures, involving silicon with varying dopant concentrations, when the distance of separation is from 10 μm down to 1 nm. The net radiation heat flux is calculated by means of the fluctuational electrodynamics. The dielectric function of silicon is modeled using a Drude model, considering the effects of temperature and doping level on the carrier concentrations and scattering times. The calculated results show that the dopant concentration strongly affects the radiation heat flux when the two media are separated at nanometer distances. For heavily doped silicon plates separated at a distance of 1 nm, the present study predicts a radiation energy flux of over five orders of magnitude greater than that between two blackbodies placed far apart. Furthermore, the radiation energy flux can be more than ten times larger than the conduction heat flux of air at the atmospheric pressure, and the radiation heat transfer coefficient may exceed 1 MW m^{-2} K^{-1}. The theoretical understanding gained from the present research will facilitate the design of experiments that utilize near-field radiation to enhance heating or cooling at the nanoscale for applications such as thermal control in nanoelectronics, energy conversion, and nanothermal probing and manufacturing.

Keywords: Microscale and nanoscale; Near-field thermal radiation; Fluctuational electrodynamics; Doped silicon

1. Introduction

Radiation heat transfer between two thermally emitting objects at short distances, when the vacuum gap separating the two solids becomes smaller than the characteristic wavelength of thermal radiation, depends on the distance of separation [1,2]. This is a distinct feature between near-field and far-field radiation heat transfer. The spacing effect is a combined result of wave interference and photon tunneling (due to evanescent waves). The effect of wave interference can be understood by plotting the spectral transmittance of a thin dielectric film versus the film thickness and observing the oscillations of transmittance due to constructive and destructive interferences [3,4]. An evanescent wave can arise from total internal reflection when light is incident from a prism to a vacuum at incidence angles greater than the critical angle. Although no energy is transferred into the vacuum, there exists an electromagnetic field that decays exponentially away from the interface. When another prism is brought to close vicinity of the first one, a backward evanescent wave emerges due to reflection at the surface of the second prism. Part of the incident energy will transmit into the second prism via interaction of the two evanescent waves that decay in opposite directions. From the particle point of view, photons (i.e., light corpuscles) can tunnel through the vacuum spacing, and the probability of tunneling increases as the spacing is reduced. For conducting or absorbing materials, there exist additional evanescent waves (or modes) that can transmit the energy of the thermally induced fluctuating electromagnetic fields from one object to another at very short distances [5]. Therefore, at nanometer distances, the effect of photon tunneling may dominate the energy transfer process so that the

* Corresponding author. Tel.: +1 404 385 4225; fax: +1 404 894 8496.
E-mail address: zhuomin.zhang@me.gatech.edu (Z.M. Zhang).

0017-9310/$ - see front matter © 2005 Elsevier Ltd. All rights reserved.
doi:10.1016/j.ijheatmasstransfer.2005.09.037

Nomenclature

c	speed of light in vacuum, 2.998×10^8 m s^{-1}
D	density of states, s rad^{-1} m^{-3}
d	vacuum gap thickness, m
$\mathbf{E}$	electric field vector, V m^{-1}
e	electron charge, 1.602×10^{-19} C
$\overline{\overline{\mathbf{G}}}$	dyadic Green function, m^{-1}
$\mathbf{H}$	magnetic field vector, A m^{-1}
h_r	radiation heat transfer coefficient, W m^{-2} K^{-1}
$\hbar$	Planck's constant over 2π, 1.055×10^{-34} J s
$\overline{\overline{\mathbf{I}}}$	unit dyadic
$\mathbf{j}$	fluctuating electric current density, A m^{-2}
$\mathbf{k}$	wavevector, m^{-1}
k_B	Boltzmann's constant, 1.381×10^{-23} J K^{-1}
m^*	effective mass, kg
m_0	electron rest mass, 9.109×10^{-31} kg
N	concentration (number density), m^{-3}
n	refractive index
q''_{net}	net energy flux, W m^{-2}
q''_ω	spectral energy flux, W m^{-2} s rad^{-1}
$\mathbf{r}$	vector in the radial direction, m
r	reflection coefficient
$\mathbf{S}$	Poynting vector, W m^{-2}
T	temperature, K
t	transmission coefficient
u	energy density, J m^{-3}
u_ω	spectral energy density, J m^{-3} s rad^{-1}
$Z(\beta)$	exchange function defined in Eq. (11)

Greek symbols

α	absorption coefficient, $\alpha = 4\pi\kappa/\lambda$, m^{-1}
β	parallel wavevector component, m^{-1}
γ	wavevector component in z-direction, m^{-1}
ε	relative permittivity (i.e., dielectric function)
ε_0	permittivity of vacuum, 8.854×10^{-12} F m^{-1}
Θ	mean energy of an oscillator, J
κ	extinction coefficient
λ	wavelength in vacuum, m
μ	mobility, cm^2 V^{-1} s^{-1}
μ_0	permeability of vacuum, $4\pi \times 10^{-7}$ H m^{-1}
ρ	reflectivity at the interface
τ	carrier scattering time, s
ω	angular frequency, rad s^{-1}

Subscripts

0	vacuum
1	medium 1
2	medium 2
A	acceptor
D	donor
d	defect
e	electron
evan	evanescent wave
h	hole
l	lattice
prop	propagating wave

Superscripts

0	value at 300 K
p	p polarization
s	s polarization

net heat flux will be much greater than that predicted by the Stefan–Boltzmann law between two blackbodies separated at large distances [5–10].

Nanoscale thermal radiation has important applications in microscale energy conversion devices [11–13] and in near-field scanning thermal microscopy [14–17]. Recent studies of negative index materials suggested some unique opportunities that could be used to enhance photon tunneling through longer distances [18,19]. The calculation of near-field radiation heat transfer between dielectric materials is rather straightforward [1,4,11]. Most of the theoretical works were performed on the prediction of the net heat flux between two parallel metallic plates using a Drude model for the dielectric function [5,7–10]. Several studies also considered the nanoscale energy transfer between a sphere and a surface [5,10,20]. Nanoscale radiation heat transfer between crystalline dielectrics can be significantly enhanced when absorption is considered [6,12,13,21,22]. This is particularly true when the dielectric materials support low-frequency surface waves or surface phonon polaritons. A surface wave is an electromagnetic wave that propagates along the interface but the amplitude decays exponentially into both media. The spectral heat flux can be enhanced by several orders of magnitude by resonance excitation of surface waves coupled with photon tunneling at the nanoscale [6,21]. While many normal metals support surface waves through surface plasmon polaritons, the plasma frequencies are usually much higher than the characteristic frequencies of thermal sources. Consequently, the near-field enhancement is not so large for good conductors. On the other hand, semi-metals, which have lower electric conductivity, may greatly enhance radiation heat flux at nanometer scales [8,9].

The interest in studying nanoscale radiation heat transfer with silicon emerges because silicon is the most extensively used material in MEMS/NEMS and many other microelectronic devices. Radiation heat transfer in these devices may be important when their characteristic dimensions are on the nanometer scales. More recently, atomic force microscope (AFM) cantilevers with integrated heaters and with nanoscale sharp tips made of doped silicon have been developed for thermal writing and reading [23].

These heated cantilever tips may provide local heating for the study of radiation energy transfer between two objects separated by a few nanometers. It is critical to quantitatively predict the near-field radiation heat flux between doped silicon. For silicon, the infrared properties are strongly dependent on the temperature and dopant concentration. Nanoscale radiation heat flux depends largely on the optical properties of the materials. Therefore, it is imperative to study the dependence of the net heat flux on the carrier concentration and scattering time, which are functions of the dopant concentration and temperature. The only work on the near-field heat transfer between doped silicon to date was given by Marquier et al. [22], who showed that heat transfer can be significantly enhanced with heavily doped silicon. However, they assumed that all the impurities are ionized (that is, the dopant concentration is the same as the carrier concentration) and did not consider the effect of temperature on the scattering time and the carrier concentration.

The present study focuses on the near-field radiation heat transfer between two closely spaced semi-infinite media with parallel and smooth surfaces, especially with doped silicon, as shown in Fig. 1a. The two media, each at thermal equilibrium but at different temperatures T_1 and T_2, are separated by a vacuum gap of width d ranging from several tens of micrometers down to 1 nm. The net radiation energy flux is calculated by means of the fluctuational electrodynamics to be discussed in the next section. For non-magnetic, homogeneous, and isotropic media, the complex dielectric function is the only property needed to fully characterize the optical behavior. However, the dielectric function is a comprehensive function of frequency and temperature for a given material. In the present study, the dielectric function of silicon is described by a Drude model, considering the effects of temperature and doping level on the concentrations and scattering times of electrons and holes. The theory of nanoscale radiation heat transfer is presented in Section 2, followed by a description of the model of the dielectric function of doped silicon in Section 3. Detailed results of radiation heat transfer for different doping levels and source temperatures are provided in Section 4, after a brief discussion on the validation of the dielectric function model. An effort is made to explain the mechanisms of heat transfer enhancement at the nanoscale and the dependence of near-field radiation on the optical properties of materials.

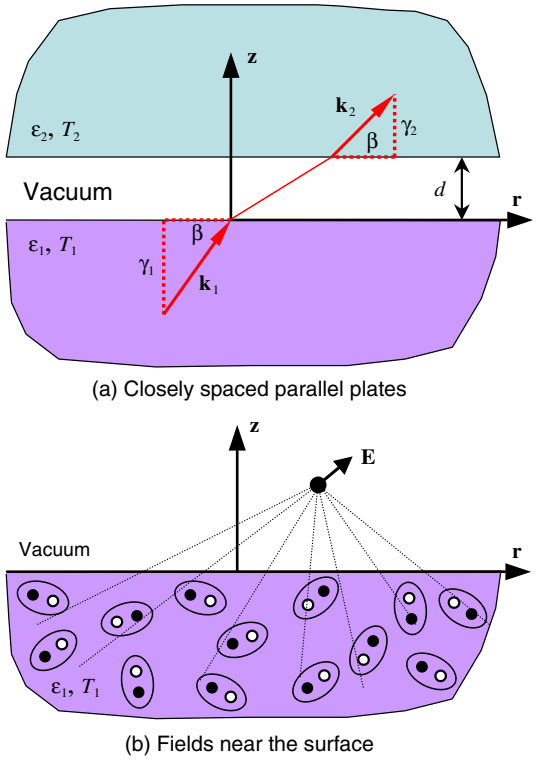

Fig. 1. Schematic drawings of the study of near-field thermal radiation: (a) radiation heat transfer between two closely spaced parallel plates separated by a vacuum gap of thickness d, and (b) the electric field near the surface due to thermally induced charge fluctuation or dipole movement. Here, cylindrical coordinates are used, and the z-direction is perpendicular to the interfaces. The wavevectors $\mathbf{k}_1$ or $\mathbf{k}_2$ are composed of β (parallel to the interfaces) and γ_1 or γ_2 (normal to the interfaces).

2. The fluctuational electrodynamics

Conventional radiation heat transfer theories [2,3] break down in the near field. The foundation of fluctuational electrodynamics is the fluctuation–dissipation theorem, in which thermal radiation is originated from the random movement of charges or dipoles inside the medium at temperatures exceeding zero kelvin. As shown in Fig. 1b, the electromagnetic field at any location is a superposition of contributions from all point sources in the radiating region. The electromagnetic waves deep inside the medium will attenuate due to absorption (i.e., dissipation) inside the medium. The fluctuational electrodynamics was established by Rytov in the 1950's (see Ref. [24]), and thereafter, has been applied by many researchers [6–10,12,13,25,26] to study near-field thermal radiation. The fluctuation–dissipation theorem has also been used to study the van der Waals forces and non-contact friction at the nanoscale [27–29]. Considering the majority of the heat transfer community may be unfamiliar with this approach, a brief derivation is provided in this section with key equations for calculating the energy density near a surface and the net heat transfer between parallel plates at different temperatures. The integral formulation will help interpret the computational results for different doping levels of silicon and in both the far-field and near-field limits. The basic assumptions used in the present study as depicted in Fig. 1 are as follows: (1) Each medium is semi-infinite and at a thermal equilibrium, presumably due to a sufficiently large thermal conductivity of the solid. (2) Both media are non-magnetic, isotropic, and homogeneous, so that the frequency-dependent complex dielectric function (relative permittivity) ε_1 or ε_2 is the only material property that characterizes the electrodynamic response and thermally induced dipole

emission of medium 1 or 2. (3) Each surface is perfectly smooth, and the two surfaces are parallel to each other.

Because of axial symmetry, cylindrical coordinates can be used so that the space variable $\mathbf{x} = \mathbf{r} + \mathbf{z} = r\hat{\mathbf{r}} + z\hat{\mathbf{z}}$. Consider a monochromatic electromagnetic wave originated from medium 1 to 2, as shown in Fig. 1a. The complex wavevectors in media 1 and 2 are $\mathbf{k}_1$ and $\mathbf{k}_2$, respectively, with $k_1^2 = \varepsilon_1 k_0^2$ and $k_2^2 = \varepsilon_2 k_0^2$, where $k_0 = \omega/c = 2\pi/\lambda$ is the magnitude of the wavevector in vacuum. Here, ω is the angular frequency, c is the speed of light in vacuum, and λ is the wavelength in vacuum. The monochromatic plane wave can be expressed in terms of a time and frequency dependent field, $e^{i\mathbf{k}_j\cdot\mathbf{x}}e^{-i\omega t}$, where $j = 0$, 1, or 2 refers to vacuum, medium 1, or medium 2, respectively. The phase matching boundary condition requires that the parallel components of all three wavevectors be the same [4]. In the present study, β is used for the parallel component of the wavevector and γ_j denotes the z-component of the wavevector $\mathbf{k}_j$. Thus $\mathbf{k}_j = \beta\hat{\mathbf{r}} + \gamma_j\hat{\mathbf{z}}$ and $\gamma_j = \sqrt{k_j^2 - \beta^2}$. Because ε_1 and ε_2 are generally complex, k_1 and k_2 may be complex. Since only real and positive frequencies (ω) are considered, k_0 is always real and positive. The spatial dependence of the field in air can be expressed as $e^{i\beta r}e^{i\gamma_0 z}$. Because the amplitude must not change along the r-direction, β must be real. Note that both r and β are positive in the cylindrical coordinates. Hence, $\gamma_0 = \sqrt{k_0^2 - \beta^2}$ will be real when $0 \leqslant \beta \leqslant \omega/c$ and purely imaginary when $\beta > \omega/c$. An evanescent wave exists in vacuum if γ_0 is imaginary, i.e., when $\beta > \omega/c$. In this case, the field will decay exponentially in the z-direction. Understanding the nature of evanescent waves is essential to the interpretation of photon tunneling and near-field radiation.

The random thermal fluctuations produce a space-time dependent electric current density $\mathbf{j}(\mathbf{x}, t)$ inside the medium whose time average is zero. It can be decomposed into the frequency domain using Fourier transform, which gives $\mathbf{j}(\mathbf{x}, \omega)$. With the assistance of the dyadic Green function, $\overline{\overline{\mathbf{G}}}(\mathbf{x}, \mathbf{x}', \omega)$, the induced electric field in the frequency domain can be expressed as a volume integration [24]:

$$\mathbf{E}(\mathbf{x}, \omega) = i\omega\mu_0 \int_V \overline{\overline{\mathbf{G}}}(\mathbf{x}, \mathbf{x}', \omega)\cdot\mathbf{j}(\mathbf{x}', \omega)d\mathbf{x}' \tag{1}$$

where μ_0 is the magnetic permeability of vacuum and the integral is over the region V that contains the fluctuating sources. The physical significance of the Green function is that it is a transfer function for a current source $\mathbf{j}$ at location $\mathbf{x}'$ and the resultant electric field $\mathbf{E}$ at $\mathbf{x}$. Mathematically, the dyadic Green function satisfies the vector Helmholtz equation,

$$\nabla\times\nabla\times\overline{\overline{\mathbf{G}}}(\mathbf{x}, \mathbf{x}', \omega) - k^2\overline{\overline{\mathbf{G}}}(\mathbf{x}, \mathbf{x}', \omega) = \overline{\overline{\mathbf{I}}}\delta(\mathbf{x} - \mathbf{x}') \tag{2}$$

where k is the amplitude of the wavevector at $\mathbf{x}$, and $\overline{\overline{\mathbf{I}}}$ is a unit dyadic. The corresponding magnetic field $\mathbf{H}(\mathbf{x}, \omega)$ can be obtained from the Maxwell equation, that is,

$$\mathbf{H}(\mathbf{x}, \omega) = \frac{1}{i\omega\mu_0}\nabla\times\mathbf{E}(\mathbf{x}, \omega) \tag{3}$$

The spectral energy density of the thermally emitted electromagnetic field in vacuum can be calculated from [30]

$$u_\omega(\mathbf{x}, \omega) = \frac{\varepsilon_0}{4}\langle\mathbf{E}(\mathbf{x}, \omega)\cdot\mathbf{E}^*(\mathbf{x}, \omega)\rangle + \frac{\mu_0}{4}\langle\mathbf{H}(\mathbf{x}, \omega)\cdot\mathbf{H}^*(\mathbf{x}, \omega)\rangle \tag{4}$$

where ε_0 is the electric permittivity of vacuum, $\langle\rangle$ denotes the ensemble average of the random currents, and $*$ signifies complex conjugate. The emitted energy flux can be expressed by the ensemble average of the Poynting vector [30], hence,

$$\langle\mathbf{S}(\mathbf{x}, \omega)\rangle = \frac{1}{2}\langle Re[\mathbf{E}(\mathbf{x}, \omega)\times\mathbf{H}^*(\mathbf{x}, \omega)]\rangle \tag{5}$$

To evaluate the ensemble average, the spatial correlation function between the fluctuating currents at two locations $\mathbf{x}'$ and $\mathbf{x}''$ inside the emitting medium is needed and is given in [24] as

$$\left\langle j_m(\mathbf{x}', \omega)j_n^*(\mathbf{x}'', \omega)\right\rangle = \frac{4\omega\varepsilon_0\,\mathrm{Im}(\varepsilon)\Theta(\omega, T)}{\pi}\delta_{mn}\delta(\mathbf{x}' - \mathbf{x}'') \tag{6}$$

where Im takes the imaginary part of the dielectric function, δ_{mn} is the Kronecker delta function, $\delta(\mathbf{x}' - \mathbf{x}'')$ is the Dirac delta function, and $\Theta(\omega, T)$ is the mean energy of a Planck oscillator at frequency ω in thermal equilibrium and given by [31]

$$\Theta(\omega, T) = \frac{\hbar\omega}{\exp(\hbar\omega/k_B T) - 1} \tag{7}$$

where $\hbar = h/2\pi$ is Planck's constant over 2π and k_B is the Boltzmann constant. In Eq. (7), the term $\hbar\omega/2$ that accounts for vacuum fluctuation is omitted since it does not affect the net radiation heat flux [31]. The calculated energy density should be regarded as being relative to the vacuum ground energy density. A factor of four has been included in Eq. (6) to be consistent with the conventional definitions of the spectral energy density and Poynting vector expressed in Eqs. (4) and (5), respectively, since only positive values of frequencies are considered here [30]. The local density of states or density of modes is defined by the following relation [25,26]:

$$u_\omega(z, \omega) = D(z, \omega)\Theta(\omega, T) \tag{8}$$

The energy density and density of states are independent of r. The physical significance of $D(z, \omega)$ [$\mathrm{m}^{-3}\,\mathrm{s\,rad}^{-1}$] is the number of modes per unit frequency interval per unit volume.

The Green function depends on the geometry of the physical system and for two parallel semi-infinite media shown in Fig. 1, it takes the following form [32]:

$$\overline{\overline{\mathbf{G}}}(\mathbf{x}, \mathbf{x}', \omega) = \frac{i}{4\pi}\int_0^\infty \frac{\beta\,d\beta}{\gamma_1}\left(\hat{\mathbf{s}}t_{12}^s\hat{\mathbf{s}} + \hat{\mathbf{p}}_2 t_{12}^p\hat{\mathbf{p}}_1\right)e^{i\gamma_2 z - i\gamma_1 z'}e^{i\beta\hat{\mathbf{r}}\cdot(\mathbf{r}-\mathbf{r}')} \tag{9}$$

where $\mathbf{x} = r\hat{\mathbf{r}} + z\hat{\mathbf{z}}$ and $\mathbf{x}' = r'\hat{\mathbf{r}} + z'\hat{\mathbf{z}}$, t_{12}^{s} and t_{12}^{p} are the transmission coefficients from medium 1 to medium 2 for s and p polarization, respectively, and the unit vectors $\hat{\mathbf{s}} = \hat{\mathbf{r}} \times \hat{\mathbf{z}}$, $\hat{\mathbf{p}}_1 = (\beta\hat{\mathbf{z}} - \gamma_1\hat{\mathbf{r}})/k_1$, and $\hat{\mathbf{p}}_2 = (\beta\hat{\mathbf{z}} - \gamma_2\hat{\mathbf{r}})/k_2$. If the interest is to calculate the radiation field from medium 1 to vacuum, t_{12}^{s} and t_{12}^{p} can be replaced by the Fresnel transmission coefficients between medium 1 and vacuum, i.e., t_{10}^{s} and t_{10}^{p}. By using Eqs. (6) and (9), one can evaluate Eqs. (1) and (3) to obtain the electric and magnetic fields; consequently, the energy density, flux, and density of states can be calculated. For example, the local density of states in vacuum near the surface medium 1 can be expressed in two terms [26]:

$$D(z,\omega) = D_{\text{prop}}(\omega) + D_{\text{evan}}(z,\omega) \tag{10}$$

where

$$D_{\text{prop}}(\omega) = \frac{\omega}{\pi^2 c^2}\int_0^{\omega/c} \frac{\beta\,\mathrm{d}\beta}{2\gamma_0}(2 - \rho_{01}^{s} - \rho_{01}^{p}) \tag{10a}$$

and

$$D_{\text{evan}}(z,\omega) = \frac{1}{\pi^2\omega}\int_{\omega/c}^{\infty} \frac{\mathrm{e}^{-2z\,\mathrm{Im}(\gamma_0)}\beta^3\,\mathrm{d}\beta}{2\mid\gamma_0\mid}[\mathrm{Im}(r_{01}^{s}) + \mathrm{Im}(r_{01}^{p})] \tag{10b}$$

where r_{01} is the Fresnel reflection coefficient and $\rho_{01} = |r_{01}|^2$ is the (far-field) reflectivity at the interface between vacuum and medium 1, superscripts s and p signify s-polarization (TE wave) and p-polarization (TM wave), respectively. Note that $r_{01}^{s} = (\gamma_0 - \gamma_1)/(\gamma_0 + \gamma_1)$ and $r_{01}^{p} = (\varepsilon_1\gamma_0 - \gamma_1)/(\varepsilon_1\gamma_0 + \gamma_1)$. It should be noted that, in deriving Eq. (10), the imaginary part of the permittivity (of medium 1) in Eq. (6) has been combined with other terms containing the relative permittivity of medium 1. It should be mentioned that no matter how small $\mathrm{Im}(\varepsilon_1)$ may be, such as for a dielectric, it must not be zero for the semi-infinite assumption to hold. The contribution of propagating waves given by Eq. (10a) is independent of z and exists in both the near and far fields; whereas the contribution of evanescent waves decreases with increasing z. In the far-field limit, the contribution of the propagating waves is responsible to thermal emission and one can see the directional-spectral emissivity term in Eq. (10a), i.e., $\varepsilon_{\omega,1}^{\prime s} = 1 - \rho_{01}^{s}$ and $\varepsilon_{\omega,1}^{\prime p} = 1 - \rho_{01}^{p}$. As z becomes smaller and smaller, the contribution of evanescent waves near the surface may dominate when $\mathrm{Im}(r_{01}^{p})$ is large as in the case of surface phonon polaritons [25], resulting in very large energy densities near the surface.

The spectral energy flux from medium 1 to medium 2 is calculated by projecting the time-averaging Poynting vector from Eq. (5) into the z-direction, and hence [6,9],

$$q''_{\omega,1-2} = \frac{\Theta(\omega,T_1)}{\pi^2}\int_0^{\infty} Z_{12}(\beta)\beta\,\mathrm{d}\beta \tag{11}$$

where

$$Z_{12}(\beta) = \frac{4\,\mathrm{Re}(\gamma_1)\mathrm{Re}(\gamma_2)\left|\gamma_0^2\mathrm{e}^{\mathrm{i}2\gamma_0 d}\right|}{\left|(\gamma_0+\gamma_1)(\gamma_0+\gamma_2)(1 - r_{01}^{s}r_{02}^{s}\mathrm{e}^{\mathrm{i}2\gamma_0 d})\right|^2} + \frac{4\,\mathrm{Re}(\varepsilon_1\gamma_1^*)\mathrm{Re}(\varepsilon_2\gamma_2^*)\left|\gamma_0^2\mathrm{e}^{\mathrm{i}2\gamma_0 d}\right|}{\left|(\varepsilon_1\gamma_0+\gamma_1)(\varepsilon_2\gamma_0+\gamma_2)(1 - r_{01}^{p}r_{02}^{p}\mathrm{e}^{\mathrm{i}2\gamma_0 d})\right|^2}$$

is called the *exchange function* in the present study. Note that Re takes the real part of the complex variable. Eq. (11) includes the contributions from both propagating waves and evanescent waves (photon tunneling). The expression of $q''_{\omega,2-1}$ is readily obtained by replacing $\Theta(\omega, T_1)$ in Eq. (11) with $\Theta(\omega, T_2)$ since the exchange function is reciprocal: $Z_{12}(\beta) = Z_{21}(\beta)$. The units of q''_{ω} is expressed as [W m^{-2} s rad^{-1}] rather than [J m^{-2} rad^{-1}] to keep the integrity of the frequency units [s rad^{-1}]. This is commonly done when wavelength [μm] is used such that the spectral radiation heat flux is expressed in [W m^{-2} μm^{-1}] [2].

The net total energy flux is the integration of $q''_{\omega,1-2} - q''_{\omega,2-1}$ over all frequencies, viz.

$$\begin{aligned} q''_{\text{net}} &= \int_0^{\infty}(q''_{\omega,1-2} - q''_{\omega,2-1})\,\mathrm{d}\omega \\ &= \frac{1}{\pi^2}\int_0^{\infty}\mathrm{d}\omega[\Theta(\omega,T_1) - \Theta(\omega,T_2)]\int_0^{\infty} Z_{12}(\beta)\beta\,\mathrm{d}\beta \end{aligned} \tag{12}$$

Eq. (12) provides an ab initio calculation of the thermal radiation that is applicable for both the near- and far-field heat transfer. The contribution of evanescent waves with imaginary γ_0 (for $\beta > \omega/c$) reduces as d increases and is negligible when d is on the order of the wavelength. The energy transfer can also be separated into contributions of propagating waves and evanescent waves (photon tunneling).

The exchange function Z can be re-written using the Fresnel coefficients and reflectivity for propagating waves as [6,9]

$$Z_{\text{prop}}(\beta) = \frac{(1-\rho_{01}^{s})(1-\rho_{02}^{s})}{4\left|1 - r_{01}^{s}r_{02}^{s}\mathrm{e}^{-\mathrm{i}2\gamma_0 d}\right|^2} + \frac{(1-\rho_{01}^{p})(1-\rho_{02}^{p})}{4\left|1 - r_{01}^{p}r_{02}^{p}\mathrm{e}^{-\mathrm{i}2\gamma_0 d}\right|^2}, \quad \beta < \omega/c \tag{13}$$

Substituting Eq. (13) into Eq. (10) and noting that $\beta = \omega/c\sin\theta$, where θ is the polar angle in vacuum, the integration can be evaluated in the far-field limit from $\theta = 0$ to $\pi/2$. Note that in the incoherent limit ($d \gg \lambda$) when the oscillation terms are averaged,

$$\frac{1}{\mid 1 - r_{01}^{s}r_{02}^{s}\mathrm{e}^{-\mathrm{i}2\gamma_0 d}\mid^2} \to \frac{1}{1 - \rho_{01}^{s}\rho_{02}^{s}} \quad [2,6]$$

It can be shown that

$$\frac{1 - \rho_{01}^{s}\rho_{02}^{s}}{(1-\rho_{01}^{s})(1-\rho_{02}^{s})} = \frac{1}{\varepsilon_{\omega,1}^{\prime s}} + \frac{1}{\varepsilon_{\omega,2}^{\prime s}} - 1$$

Similar relations hold for p-polarization. From Eq. (12), the total energy flux in the far-field limit becomes

$$q''_{\text{net,far}} = \frac{1}{4\pi^2 c^2}\int_0^\infty [\Theta(\omega,T_1)-\Theta(\omega,T_2)]\omega^2 \mathrm{d}\omega \times \int_0^{\pi/2} \cos\theta\sin\theta \mathrm{d}\theta \left(\frac{1}{1/\varepsilon'^{\mathrm{s}}_{\omega,1}+1/\varepsilon'^{\mathrm{s}}_{\omega,2}-1}+\frac{1}{1/\varepsilon'^{\mathrm{p}}_{\omega,1}+1/\varepsilon'^{\mathrm{p}}_{\omega,2}-1}\right) \tag{14}$$

Eq. (14) is similar to the equation commonly found in radiation heat transfer texts [2,3], except that angular frequency is used here instead of wavelength. The wavelength integration can be obtained by converting Planck's blackbody intensity from $\frac{\hbar\omega^3 d\omega}{4\pi^3 c^2(\mathrm{e}^{\hbar\omega/k_{\mathrm{B}}T}-1)}$ to $\frac{2hc^2 d\lambda}{\lambda^5(\mathrm{e}^{hc/k_{\mathrm{B}}\lambda T}-1)}$. While the energy flux includes the contributions by both polarizations, one should not average the surface emissivity for the s and p-polarizations and then apply the integration. Rather, one should integrate the two polarizations separately based on Eq. (14). Rigorously speaking, Kirchhoff's equality between directional-spectral emissivity and absorptivity $(1-\rho)$ [2,3] is valid only for a single polarization because the absorptivity depends also on the polarization state of the incoming radiation.

The expression of Z for the contribution of evanescent waves is [6,9]

$$Z_{\text{evan}}(\beta) = \frac{\mathrm{Im}(r^{\mathrm{s}}_{01})\mathrm{Im}(r^{\mathrm{s}}_{02})\mathrm{e}^{-2\mathrm{Im}(\gamma_0)d}}{\left|1-r^{\mathrm{s}}_{01}r^{\mathrm{s}}_{02}\mathrm{e}^{-2\mathrm{Im}(\gamma_0)d}\right|^2}+\frac{\mathrm{Im}(r^{\mathrm{p}}_{01})\mathrm{Im}(r^{\mathrm{p}}_{02})\mathrm{e}^{-2\mathrm{Im}(\gamma_0)d}}{\left|1-r^{\mathrm{p}}_{01}r^{\mathrm{p}}_{02}\mathrm{e}^{-2\mathrm{Im}(\gamma_0)d}\right|^2}, \quad \beta>\omega/c \tag{15}$$

The exchange function decays exponentially as the distance of separation d increases. Mulet et al. [6] presented a detailed comparison of the conventional radiation heat transfer theory with the fluctuational electrodynamics approach. In the present study, the term emissivity is reserved for far-field limit only without using a generalization emissivity as suggested in [6]. The introduction of the exchange function facilitates the interpretation of near-field radiation heat transfer as will be discussed later.

3. The dielectric function of silicon

The temperature range considered in the present study is from room temperature (300 K) up to 1000 K. Hence, the wavelength region of interest is from about 1 μm to the very far infrared. Silicon is an indirect semiconductor and the fundamental absorption (i.e., interband absorption) occurs at wavelengths shorter than λ_{g}, which corresponds to the band-gap energy E_{g}. For lightly doped silicon with a dopant concentration (number density) less than $10^{15}\,\mathrm{cm}^{-3}$ or a room-temperature electrical resistivity greater than 10 Ω cm, λ_{g} varies from 1.12 μm at 300 K to 1.43 μm at 1000 K [33,34]. Because photons with energy greater than the band gap can excite the electrons from the valence band to the conduction band, the absorption coefficient (α) is large at $\lambda<\lambda_{\mathrm{g}}$ and increases towards shorter wavelengths. For intrinsic silicon at low temperatures, the free carrier concentration is very low and thus silicon is transparent for $\lambda>\lambda_{\mathrm{g}}$. Lattice absorption occurs in the mid infrared and introduces some absorption for 6 μm $<\lambda<$ 25 μm. As the temperature increases, thermally excited free carriers dominate the absorption at longer wavelengths, and a 0.5-mm thick silicon wafer is essentially opaque above 1000 K. The free carrier concentration for intrinsic silicon is about $10^{10}\,\mathrm{cm}^{-3}$ at 300 K and nearly $10^{18}\,\mathrm{cm}^{-3}$ at 1000 K [34]. Free carrier absorption can also be important for doped silicon, although not all the impurities may be ionized to become free carriers. While the Drude model has been used to study intraband absorption for doped silicon in a large number of publications [22,33,35–37], the spectral and temperature regions are rather limited. It is also desirable to model the dielectric function for different doping levels. Hebb [38] initiated an effort to model the dielectric function of silicon with wide ranges of dopant concentrations, wavelength, and temperature. While the calculated absorption coefficient is consistent with published data in the near infrared at intermediate temperatures, some of the parameters are inconsistent with the well-established theory or values. Hence, the present authors have re-visited the expressions of the carrier scattering times and concentrations, resulting in a self-contained model as described below.

The complex dielectric function is related to the refractive index (n) and the extinction coefficient (κ) by $\varepsilon(\omega)=(n+\mathrm{i}\kappa)^2$, thus $\mathrm{Re}(\varepsilon)=n^2-\kappa^2$ and $\mathrm{Im}(\varepsilon)=2n\kappa$. The Drude model of the dielectric function for both intrinsic and doped silicon is given in the following [33,38]:

$$\varepsilon(\omega)=\varepsilon_{\mathrm{bl}}-\frac{N_{\mathrm{e}}e^2/\varepsilon_0 m^*_{\mathrm{e}}}{\omega^2+\mathrm{i}\omega/\tau_{\mathrm{e}}}-\frac{N_{\mathrm{h}}e^2/\varepsilon_0 m^*_{\mathrm{h}}}{\omega^2+\mathrm{i}\omega/\tau_{\mathrm{h}}} \tag{16}$$

where the first term on the right $\varepsilon_{\mathrm{bl}}$ accounts for contributions by transitions across the band gap and lattice vibrations, the second term is the Drude term for transitions in the conduction band (free electrons), and the last term is the Drude term for transitions in the valence band (free holes). Here, N_{e} and N_{h} are the concentrations, m^*_{e} and m^*_{h} the effective masses, and τ_{e} and τ_{h} the scattering times of free electrons and holes, respectively, and e is the electron charge. In the present study, the effective masses are assumed to be independent of frequency, dopant concentration, and temperature. Their values are taken from [35] as $m^*_{\mathrm{e}}=0.27m_0$ and $m^*_{\mathrm{h}}=0.37m_0$, where m_0 is the electron mass in vacuum.

Since $\varepsilon_{\mathrm{bl}}$ accounts for contributions other than the free carriers, it can be determined based on the refractive index and extinction coefficient for intrinsic silicon, i.e., $\varepsilon_{\mathrm{bl}}=(n_{\mathrm{bl}}+\mathrm{i}\kappa_{\mathrm{bl}})^2$. The modification of the band structure by impurities is neglected in the present work and this assumption should not cause significant error [38]. The refractive index of intrinsic silicon changes from about 3.6 at $\lambda=1$ μm to about 3.42 for wavelengths longer than 10 μm at room temperature and increases slightly as the temperature increases. The free carrier contribution to the refractive index of intrinsic silicon is negligibly small even

at 1000 K. Li [39] performed an extensive review of the refractive index of silicon and fitted the available data with an expression that is applicable for wavelength region between 1.2 and 14 μm at temperatures up to 750 K. In the present study, Li's expression is used for n_{bl} and extrapolated to $\lambda = 1$ μm and for temperatures up to 1000 K, as recommended by Timans [33] and more recently by Lee et al. [40]. The equations for calculating the refractive index were included in [33,40] besides Li's original publication [39] and will not be repeated here. It is assumed that n_{bl} is independent of wavelength beyond 10 μm. It should be noted that due to the weakness of the phonon oscillators in silicon, lattice vibrations contribute little to the refractive index.

The absorption coefficient due to band-gap absorption for $\lambda < \lambda_g$ has been obtained by Timans [41] following the original work of MacFarlane et al. [42]. The equations for the absorption coefficient can be found from Timans [33,41] and using the relation $\alpha = 4\pi\kappa/\lambda$, κ_{bl} at short wavelengths can be calculated for all temperatures. Some absorption by lattice vibrations occurs in silicon at wavelengths between 6 and 25 μm. At high temperatures or for heavily doped silicon, the effect of absorption by lattice vibrations is negligible compared to the absorption by free carriers. To account for lattice absorption, κ_{bl} can be obtained from the tabulated extinction coefficient values given in [43] for a slightly doped silicon sample at room temperature. A Fourier-transform infrared spectrometer was used to measure the transmittance of a single-crystal ⟨100⟩ silicon wafer of 200-μm thickness and with a resistivity exceeding 1000 Ω cm. The measured transmittance compares well with that calculated using the refractive index and extinction coefficient data from [43], although the calculated transmittance is slightly lower near 16 μm, suggesting that impurities might have affected the reported extinction coefficient. Since the effect of lattice absorption on the radiation heat transfer is insignificant, the values from [43] are used in the present study and are assumed independent of temperature and dopant concentration. Although the Drude terms contribute little to the dielectric function of lightly doped silicon at room temperature, free carriers provide non-zero Im(ε) at all frequencies as required by fluctuation–dissipation theorem discussed in the previous section.

The remaining parameters are the carrier concentrations and scattering times, which are functions of temperature and dopant concentrations. The scattering time τ_e or τ_h depends on the collisions of electrons or holes with lattice (phonons) and ionized dopant sites (impurities or defects). The total scattering time, for the case of τ_e, can be calculated by [34]

$$\frac{1}{\tau_e} = \frac{1}{\tau_{e\text{–}l}} + \frac{1}{\tau_{e\text{–}d}} \tag{17}$$

where $\tau_{e\text{–}l}$ and $\tau_{e\text{–}d}$ denote the electron–lattice and electron–defect scattering times. Similarly, τ_h can be related to $\tau_{h\text{–}l}$ and $\tau_{h\text{–}d}$. At room temperature, the following expressions can be obtained from the fitted equations for the mobilities using the relation $\tau = m^*\mu/e$, where μ is the mobility [44]:

$$\tau_e^0 = \frac{19.5}{1 + (N_D/1.3\times 10^{17})^{0.91}} + 141 \tag{18a}$$

and

$$\tau_h^0 = \frac{94}{1 + (N_A/1.9\times 10^{17})^{0.76}} + 10 \tag{18b}$$

where superscript 0 denotes values at 300 K, the scattering time is in fs (10^{-15} s), and N_D and N_A are the dopant concentrations of donor (n-type) such as phosphorus and acceptor (p-type) such as boron and are in cm^{-3}. The lattice contribution, which is independent of the carrier density, can be obtained from the room temperature lattice mobilities of 1451 cm^2 V^{-1} s^{-1} for electrons and 502 cm^2 V^{-1} s^{-1} for holes [45]. Therefore, $\tau_{e\text{–}l}^0 = 2.23\times 10^{-13}$ s and $\tau_{h\text{–}l}^0 = 1.06\times 10^{-13}$ s. The values of $\tau_{e\text{–}d}^0$ and $\tau_{h\text{–}d}^0$ depend on dopant concentrations and can be solved by combining Eqs. (17) and (18). Note that a smaller scattering time means a higher scattering rate ($1/\tau$). The scattering process is dominated by lattice scattering for lightly doped silicon, and impurity scattering becomes important when the dopant concentration exceeds 10^{18} cm^{-3}.

The temperature dependence of the scattering time is more complicated. Theory predicted that the carrier-impurity scattering times vary with $T^{1.5}$ and the carrier-lattice scattering times due to acoustic phonons vary with $T^{-1.5}$ [34]. As the temperature increases, the scattering rate due to impurity tends to decrease because the electrostatic force that governs dopant sites becomes weaker and carriers can move more agilely. On the other hand, the carrier-lattice scattering rate increases as the temperature goes up because of the increased phonon number density (occupation number). Therefore, lattice scattering dominates the scattering process at high temperatures even for heavily doped silicon. Because of the relatively insignificance of impurity scattering at high temperatures, the following formula can be used to calculate the impurity scattering times.

$$\frac{\tau_{e\text{–}d}}{\tau_{e\text{–}d}^0} = \frac{\tau_{h\text{–}d}}{\tau_{h\text{–}d}^0} = \left(\frac{T}{300}\right)^{1.5} \tag{19}$$

where T is in K. The temperature dependence of $\tau_{e\text{–}l}$ and $\tau_{h\text{–}l}$ can be more complicated since optical phonon modes may contribute to the scattering in addition to acoustic phonon modes. Morin and Maita [45] fitted the mobility with experiments and indicated that the mobility due to lattice scattering varies as $T^{-2.6}$ for electrons and $T^{-2.3}$ for phonons. In order to obtain a better agreement with the measured near-infrared absorption coefficients for lightly-doped silicon [33,38,46–48], the expressions for lattice scattering are modified in the present study as follows:

$$\tau_{e\text{–}l} = \tau_{e\text{–}l}^0 (T/300)^{-3.8} \tag{20a}$$

and

$$\tau_{h\text{–}l} = \tau_{h\text{–}l}^0 (T/300)^{-3.6} \tag{20b}$$

Substituting Eqs. (19) and (20) into Eq. (17) yields the scattering time for any temperature and dopant concentrations.

The carrier concentrations N_e and N_h in Eq. (16) depend on temperature and dopant concentrations. For intrinsic silicon, the thermally excited free electrons and holes are the same and given by [49]

$$N_{th}^2 = N_C N_V \exp(-E_g/k_B T) \tag{21}$$

where N_C and N_V, which are proportional to $T^{3/2}$, are the effective densities of states in the conduction band and valence band, respectively, and $E_g = 1.17 - 0.000473T^2/(T+636)$ eV [49]. From the more recent book of Sze [50], $N_C = 2.86\times10^{19}\,\mathrm{cm}^{-3}$ and $N_V = 2.66\times10^{19}\,\mathrm{cm}^{-3}$ at 300 K. When the dopant concentrations are not too high, the free carrier concentrations can be obtained from [34,50],

$$N_e = \frac{1}{2}\left[N_D - N_A + \sqrt{(N_D - N_A)^2 + 4N_{th}^2}\right] \tag{22a}$$

and $N_h = N_{th}^2/N_e$ when the majority impurities are n-type. On the other hand, when the majority impurities are p-type,

$$N_h = \frac{1}{2}\left[N_A - N_D + \sqrt{(N_A - N_D)^2 + 4N_{th}^2}\right] \tag{22b}$$

and $N_e = N_{th}^2/N_h$.

Eq. (22) was derived based on complete ionization, which does not hold for heavily doped semiconductors or at very low temperatures [50]. Furthermore, for n-type semiconductors when $N_D \geqslant N_C$, the Fermi level is above the bottom of the conduction band; while for p-type semiconductors when $N_A \geqslant N_V$, the Fermi level is below the top of the valence band. In this case, the semiconductor is said to be degenerated and a complicated integration is needed to obtain the Fermi energy, carrier concentrations, and the ionized impurity concentrations [34]. In addition to E_g, N_C, and N_V, the ionization energies are needed to perform the integration. The ionization energy is set to be 44 meV for n-type (phosphorous) and 45 meV for p-type (boron) doping [34]. These values can be changed for different kinds of impurities. In the present study, the dependence of the ionization energy on the doping level and temperature is neglected for simplicity. The charge neutrality requires that the total positive charges (holes and ionized donors) be equal to the total negative charges (electrons and ionized acceptors). In the present work, the procedure and approximate equations described in [51] are used to evaluate N_e and N_h for any given doping concentrations and temperature regardless of the degenerate state. The results are within 3% of the values obtained by numerical integration.

4. Results and discussion

4.1. Properties of silicon

It is helpful to understand how the properties of silicon change with the doping level and temperature, in order to analyze and interpret the nanoscale thermal radiation for silicon devices. The scattering rates τ_e and τ_h are calculated using the procedure described in the previous section as functions of N_D and N_A, respectively. The results are shown in Fig. 2 at different temperatures. Generally speaking, $\tau_e > \tau_h$, suggesting that scattering rate of holes is higher than that of electrons. This is consistent with the fact that the electron mobility is greater than the hole mobility. At temperatures greater than 700 K, scattering by impurities is negligible and the scattering time is independent of the dopant concentration. The effect of doping on the scattering time is also negligible for lightly doped silicon but impurities cause additional scattering at 300 K when the dopant concentration is greater than $10^{16}\,\mathrm{cm}^{-3}$. As the temperature increases, lattice scattering is enhanced and this causes a reduction of the scattering time. It is interesting to notice the cross-over at $N_D \approx 8.5\times10^{18}\,\mathrm{cm}^{-3}$ between the two τ_e curves for 300 and 500 K. This is because, at this doping level, the effect of enhanced lattice scattering has been canceled out by the effect of reduced impurity scattering as the temperature increases from 300 to 500 K.

The carrier concentrations are shown in Fig. 3 as functions of the donor concentration at different temperatures. In the present study, only a single type of dopant is considered. For p-type silicon, the dependence of carrier concentration upon the acceptor concentration is similar except that the majority of the carriers are holes rather than electrons. For intrinsic silicon, $N_e = N_h = N_{th}$ and increases with temperature. At temperatures below 500 K when $10^{11}\,\mathrm{cm}^{-3} < N_D < 10^{17}\,\mathrm{cm}^{-3}$, the electron concentration is almost the same as the donor concentration, suggesting a complete ionization and a much smaller contribution of the thermally excited carriers. As the dopant concentration increases, the fraction of ionization reduces and not all the donors may be ionized to become free electrons. The hole concentration decreases with increasing donors as required

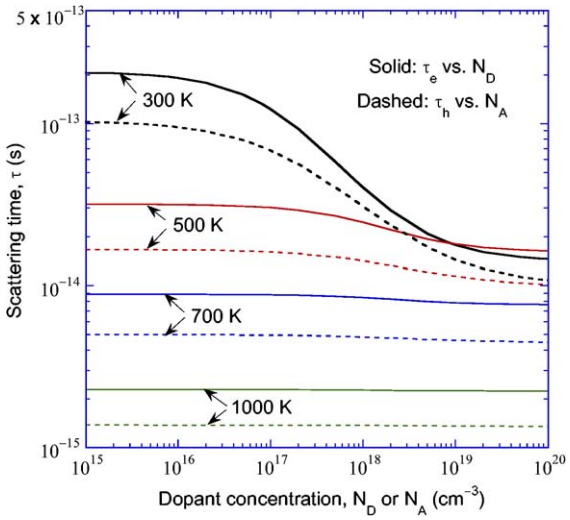

Fig. 2. Scattering times, τ_e and τ_h, as functions of the dopant concentrations, N_D and N_A, respectively, at different temperatures.

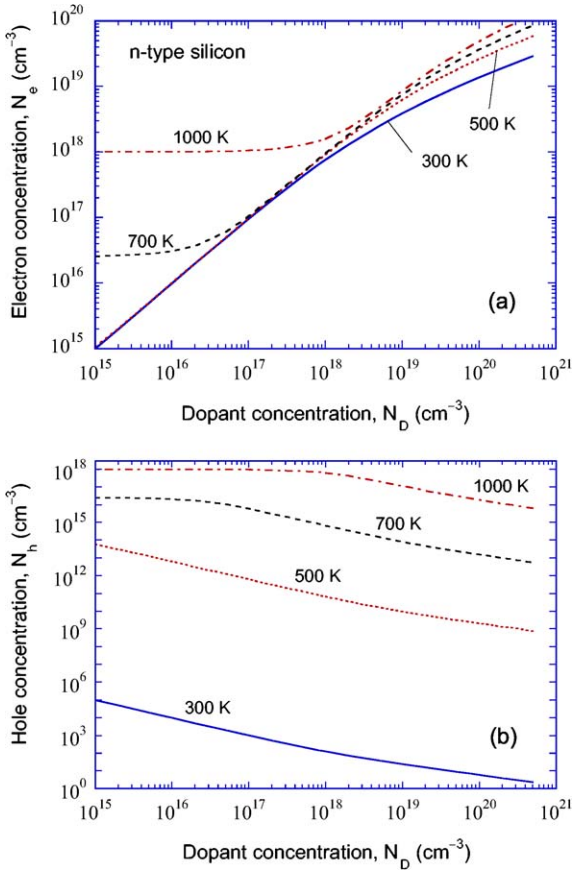

Fig. 3. Free carrier concentrations versus doping level for n-type silicon at different temperatures: (a) electron concentration; (b) hole concentration.

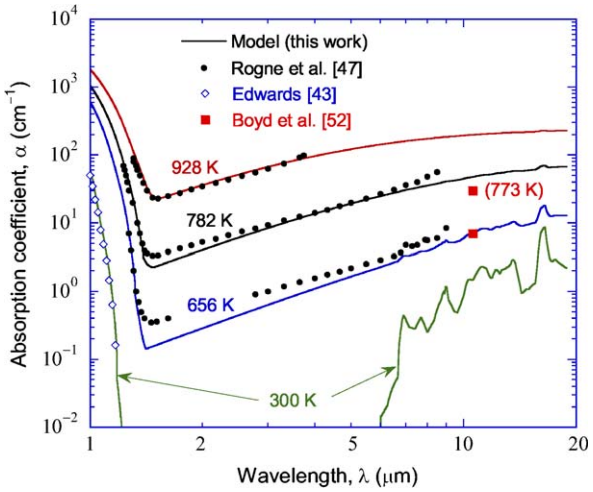

Fig. 4. Comparison of the spectral absorption coefficient of lightly doped silicon with published data at different temperatures. Note that the data of Boyd et al. [52] was obtained at 773 K (upper points) and interpolated for 656 K (lower points).

by the charge neutrality. At elevated temperatures, thermally excited free carrier may dominate for lightly doped silicon. At 1000 K, $N_e \approx N_h \approx N_{th}$ when $N_D < 5 \times 10^{17}$ cm^{-3}. For heavily doped silicon, however, the fraction of ionized electrons increases with temperature.

For intrinsic silicon or for lightly doped silicon at high temperatures, N_e and N_h are essentially the same; hence, the hole contribution will be slightly greater than the electron contribution to the dielectric function given in Eq. (16) because $\tau_e > \tau_h$. Nevertheless, the contribution of electrons and holes are of the same order of magnitude and both terms must be included. For doped silicon near room temperature and for very heavily doped silicon at high temperatures, the majority of the carriers will dominate the absorption process and the dielectric function, because the carrier concentration will be very different. In order to verify the dielectric function model, the predicted absorption coefficient of lightly doped silicon is compared with published data as shown in Fig. 4. The data for lightly doped silicon from Rogne et al. [47] are consistent with the models and data presented in [33,46,48]. The room temperature absorption coefficient due to band-gap absorption is compared with Edwards [43] and the lattice contribution was extracted directly from [43]. At room temperature, the absorption coefficient is very small and depends strongly on the dopant concentration for λ between 1.2 and 6 μm, where few reliable measurements exist. In the intermediate temperature, the agreement of the present model with the experimental data is not as good as that of the empirical relation [47]. However, the empirical relation proposed by Vandenabeele and Maex [46] to model free carrier absorption is only for wavelengths below 9 μm or so [33]. Also shown in Fig. 4 are data for lightly doped silicon at $\lambda = 10.6$ μm from Boyd et al. [52]: the upper one was for 773 K and the lower one was interpolated to 656 K. These two data points suggest that the trend in the spectral absorptance by Rogne et al. [47] may not necessarily continue towards longer wavelengths.

The predicted absorption coefficient for heavily doped silicon is in reasonable agreement with the data given by Schumann et al. [53] in the mid-infrared region at room temperature and by Sturm and Reaves [48] at $\lambda = 1.3$ μm and 1.55 μm at elevated temperatures. The results will not be shown here due to space consideration. It should not be expected that the simple Drude model given in Eq. (16) with limited parameters will describe the dielectric function of silicon perfectly. Note that the effective mass may depend on the temperature, dopant concentration, and even frequency. The scattering rate may be frequency dependent as well. Furthermore, the band structure of silicon may be modified for heavily doped silicon. Nevertheless, the present model has captured the essential features of the dielectric function of silicon, for wavelengths greater than approximately 1 μm, at temperatures from 300 to 1000 K, and with a doping level up to 10^{21} cm^{-3}.

The calculated optical constants, n and κ, of silicon for wavelengths between 1 and 100 μm are shown in Fig. 5 at 300 and 1000 K for an n-type dopant. In this spectral region, the refractive index changes little for lightly doped silicon even at high temperatures. The refractive index is independent of the dopant concentration for lightly doped

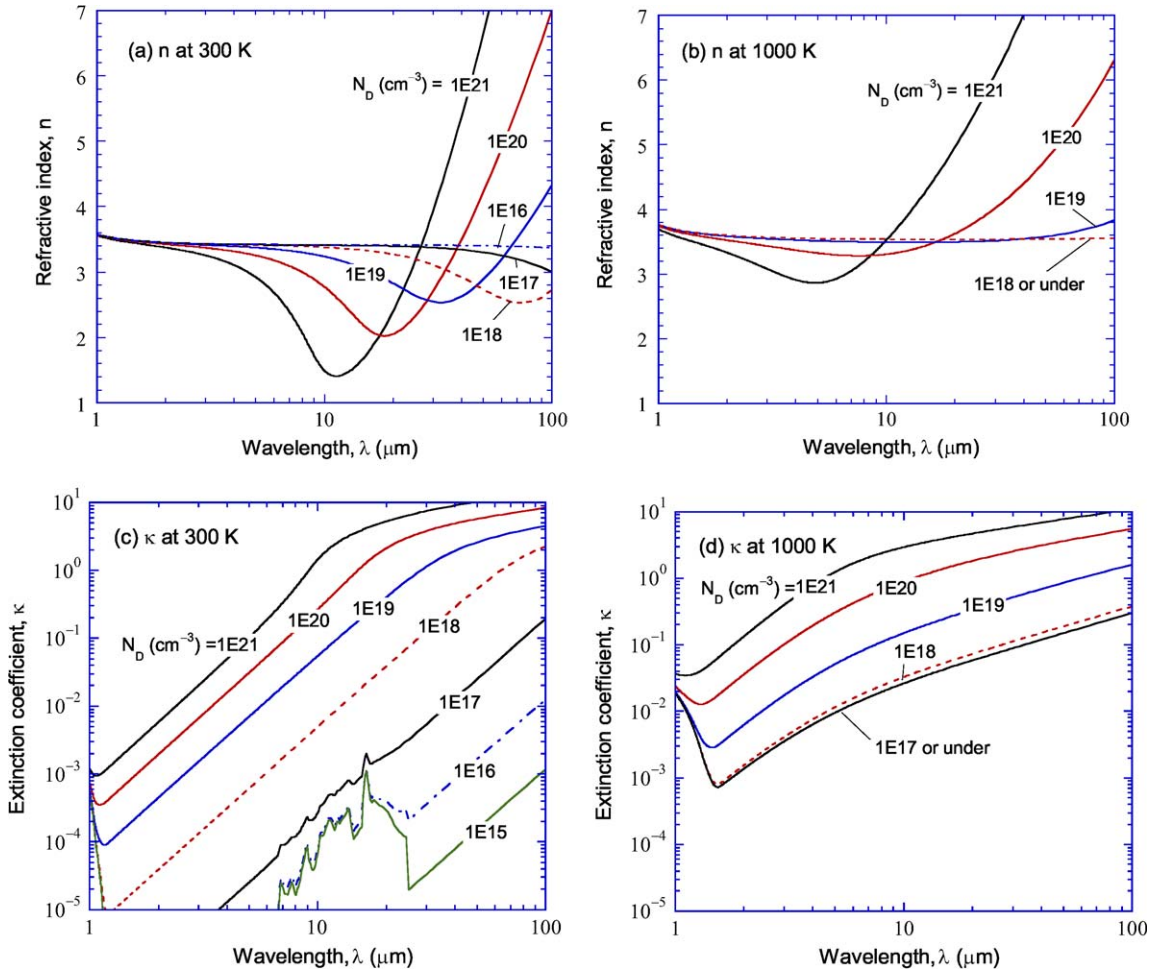

Fig. 5. Calculated optical constants of n-type silicon for different doping levels: (a) refractive index at 300 K; (b) refractive index at 1000 K; (c) extinction coefficient at 300 K; (d) extinction coefficient at 1000 K.

silicon ($N_D \leqslant 10^{15}\,cm^{-3}$) at 300 K and for N_D up to $10^{18}\,cm^{-3}$ at 1000 K. The refractive index first decreases and then increases rapidly towards longer wavelengths for heavily doped silicon. This trend agrees with the measured results [53]. The carrier contribution to the extinction coefficient at 300 K is very small for lightly doped silicon and the lattice contribution can be clearly seen. As the doping level exceeds $10^{17}\,cm^{-3}$, the phonon features have been screened out. This is also true for lightly doped silicon at 1000 K as the thermally excited carriers have a concentration of near $10^{18}\,cm^{-3}$. At 1000 K, κ is essentially the same for $N_D \leqslant 10^{17}\,cm^{-3}$ and starts to increases with increasing dopant concentration. At 300 K, however, except for the interband absorption ($\lambda < 1.12\,\mu m$) and in the lattice absorption region ($6\,\mu m < \lambda < 25\,\mu m$), the calculated κ will continue to decrease with reducing dopant concentration until it is below $10^{10}\,cm^{-3}$ when most of the carriers are due to thermal excitation rather than the doping. The significance is that the penetration depth, which is the inverse of the absorption coefficient, will be very large for very small κ. In order for the silicon plate to be approximated as a semi-infinite medium, the thickness must be much greater than $\alpha^{-1} = \lambda/4\pi\kappa$. Generally speaking, for doping level under $10^{18}\,cm^{-3}$, $\kappa \ll n$ except for very long wavelengths. This suggests that the real part of the dielectric function is much greater than the imaginary part, that is $\mathrm{Re}(\varepsilon) \gg \mathrm{Im}(\varepsilon)$. For very heavily doped silicon, on the other hand, the Drude model predicts that in the long-wavelength limit, $n \approx \kappa$; thus $\mathrm{Im}(\varepsilon) \gg \mathrm{Re}(\varepsilon)$. Because the optical constants for p-type silicon are very similar, in the present work, only n-type silicon is considered for the calculation of radiation heat transfer.

4.2. Nanoscale radiation for silicon

To calculate radiation energy flux, it is essential to evaluate the integration of the exchange function $Z_{12}(\beta)$ over wavevector β from 0 to infinity, see Eq. (11), as well as the integration of the spectral energy flux over all frequencies, see Eq. (12). The integration over β from 0 to ω/c corresponds to radiation heat transfer by propagating waves and $Z_{12}(\beta)$ is expressed as $Z_{\mathrm{prop}}(\beta)$ given in Eq. (13). In this range the integrand exhibits highly oscillatory behavior for large d. Simpson's method is an effective technique in deal-

ing with oscillatory integrands [13]. In the present study, Simpson's method is used to carry out all the integrations. The integration over β with the values of β from ω/c to infinity corresponds to radiation heat transfer by evanescent waves or photon tunneling. The exchange factor is given as $Z_{\text{evan}}(\beta)$ in Eq. (15). For small d values, the upper limit $\beta_{\max}$ should be on the order of $1/d$ [5,9]; but for large d values, $1/d$ would be less than ω/c. In the present study, $\beta_{\max}$ is chosen as $3/d$ or $100\omega/c$, whichever is larger, to ensure an integration error less than 1%. An effective way to perform the integration is to break it into several parts and evaluate each part using Simpson's rule. For example, the integration can be carried out in two parts, $\omega/c < \beta < 6\omega/c$ and $6\omega/c < \beta < \beta_{\max}$. A relative difference of 0.1% is used as the convergence criterion between consecutive iterations.

For conventional radiation heat transfer calculations, the lower and upper bounds of the integration over frequency (or wavelength) can be selected such that 99% of the blackbody emissive power falls between the limits. For example, 99% of blackbody radiation emissive power is concentrated between 1.2 and 25 μm at 1000 K and between 4 and 85 μm at 300 K [2]. For silicon, the enhancement of near-field radiation heat transfer is generally greater at longer wavelengths and thus the integration should be performed over a broader spectral region. In the present study, the wavelength region was chosen from 0.94 μm to about 1.88 mm (ω from 10^{12} to 2×10^{15} rad s^{-1}).

Assuming that the dielectric functions are exact, the overall computational uncertainty is less than 3%. The validation of the computational code was performed by comparing the energy fluxes obtained from this study with existing works, including those for two SiC media [6] and two metallic media [7] using appropriate dielectric function models. The program is in Matlab and runs on a personal computer. It generally takes less than 30 minutes to evaluate the total energy flux at a given distance for specific temperatures and doping conditions with a computer speed of 3.2 GHz.

Fig. 6 shows the predicted radiation heat transfer between two silicon plates. Medium 1 is intrinsic silicon at $T_1 = 1000$ K, whereas medium 2 is at $T_2 = 300$ K and its doping levels vary from intrinsic to heavily doped. The dotted line is the far-field radiation heat flux between two blackbodies, $\sigma(T_1^4 - T_2^4)$, predicted by the Stefan–Boltzmann law. Wien's displacement law [2] suggests that the dominant wavelength $\lambda_{\max}$ for the 1000 K emitter is around 3 μm. The energy flux is essentially a constant when the distance d is greater than 10 μm, which is the far-field regime. The net energy flux increases quickly when $d < \lambda_{\max}$ due to photon tunneling. When medium 2 is intrinsic or lightly doped, $N_{D2} < 10^{15}\,\text{cm}^{-3}$, the maximum q''_{net} is reached at $d \approx 50$ nm and changes little with further reduction of d. The maximum net energy flux is 21.3 times that of the far-field limit and 11.7 times that with blackbodies for intrinsic silicon. On the other hand, q''_{net} for $N_{D2} > 10^{16}\,\text{cm}^{-3}$ continues to increase as d is reduced and will not saturate. Since the results for $N_{D2} = 10^{17}$, 10^{19}, and $10^{20}\,\text{cm}^{-3}$ are very similar to that for $N_{D2} = 10^{18}\,\text{cm}^{-3}$, only the last case is shown in the figure. The heat flux at $d = 1$ nm with $N_{D2} = 10^{18}\,\text{cm}^{-3}$ is 800 times greater than that between two blackbodies.

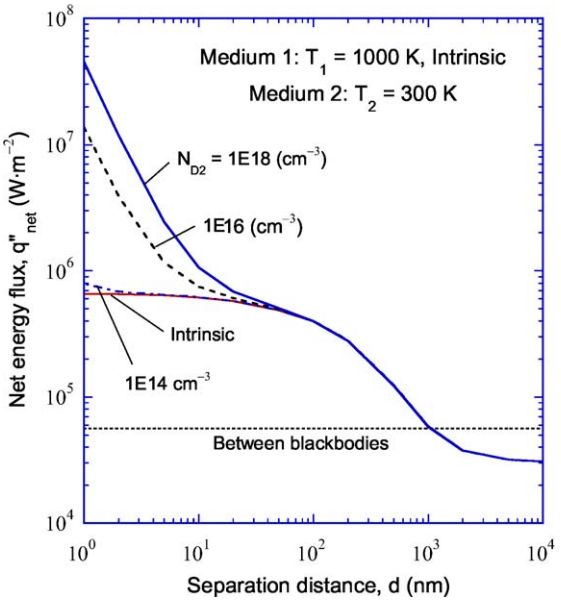

Fig. 6. Net energy flux between a 1000 K intrinsic silicon (medium 1) and a 300 K silicon (medium 2) with different doping levels as a function of the distance of separation.

If one of the media is a slightly absorbing dielectric, as for silicon with a carrier concentration less than $10^{15}\,\text{cm}^{-3}$, the Fresnel coefficients beyond the critical angle become imaginary because there is a propagating wave in the medium and an evanescent wave in vacuum (corresponding to frustrated total internal reflection). If the refractive index of the dielectric medium is n, then $Z_{\text{evan}}(\beta)$ will be non-zero for $\omega/c < \beta < n\omega/c$. However, because κ is negligibly small, $Z_{\text{evan}}(\beta)$ will be very small beyond $n\omega/c$ and decay exponentially with increasing β. Therefore, for lightly doped silicon, the enhancement is limited to approximately $(n^2-1)\sigma(T_1^4 - T_2^4)$ and the near-field flux becomes $q''_{\text{net}} \approx n^2\sigma(T_1^4 - T_2^4)$, as shown in earlier works [1,11]. Because of the small difference between the refractive indices of the two media, here, n is used for both media for simplicity. On the other hand, if κ is not so small, the integration over $\beta > n\omega/c$ may have a significant contribution to the heat flux and eventually dominates the heat flux when the distance d reaches a few nanometers, which is the case for $N_{D2} > 10^{15}\,\text{cm}^{-3}$.

The enhancement of near-field heat transfer can be better understood by looking at the energy flux spectra shown in Fig. 7. Notice that at 1000 K, the carrier concentration is about $10^{18}\,\text{cm}^{-3}$. The spectral flux between two blackbodies at 1000 K and 300 K calculated from Planck's spectral emissivity power [2,3] is also shown for comparison. Interferences become important at $d = 10$ μm and cause the

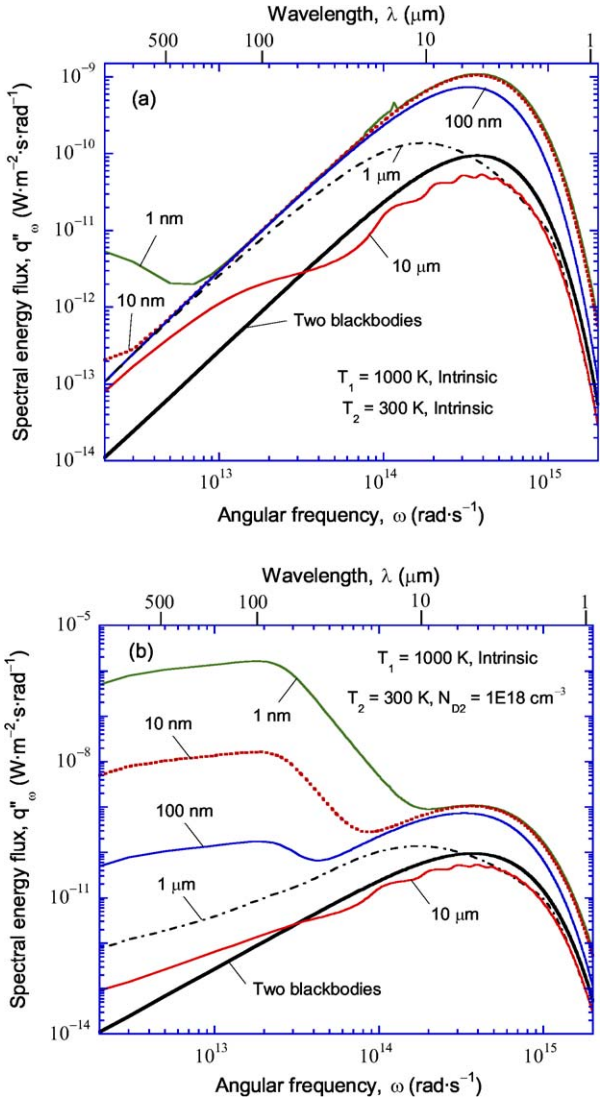

Fig. 7. Spectral energy flux for different separation distances between an intrinsic silicon at $T_1 = 1000$ K and medium 2 at $T_2 = 300$ K: (a) medium 2 is intrinsic silicon; (b) medium 2 is n-type silicon with a donor concentration $N_{D2} = 10^{18}\,\mathrm{cm}^{-3}$.

wavy features in the spectral energy flux. When the receiver is intrinsic, as shown in Fig. 7a, the shape of the spectrum is similar at $d < 100$ nm and scaled up with n^2 (≈ 11.7) times that of the blackbody. However, the slightly increased κ due to phonon absorption and in the far-infrared due to free carriers can result in an increase in the spectral energy flux, while the increase is not significant enough to vary the total flux. The near-field spectral flux is greatly enhanced with doping as can be seen from Fig. 7b, especially in the far-infrared region. As mentioned earlier, the increased energy flux in the longer wavelengths requires the integration to be carried out much broader than that of blackbody spectrum. The mechanism underlying the nanoscale enhancement is discussed below.

At the nanometer scale when near-field radiation dominates for doped silicon, the exchange factor from Eq. (15) can be simplified. When $\beta \gg \omega/c$, $\gamma_1 \approx \gamma_2 \approx \gamma_0 \approx \mathrm{i}\beta$. In this case, r_{01}^{s} and r_{02}^{s} are negligibly small so that the contribution of s-polarized waves can be neglected. Furthermore,

$$r_{01}^{\mathrm{p}} \approx \frac{\varepsilon_1 - 1}{\varepsilon_1 + 1} \quad \text{and} \quad r_{02}^{\mathrm{p}} \approx \frac{\varepsilon_2 - 1}{\varepsilon_2 + 1}$$

are independent of β. Therefore,

$$Z_{\mathrm{evan}}(\beta) \approx \frac{\mathrm{Im}(r_{01}^{\mathrm{p}})\mathrm{Im}(r_{02}^{\mathrm{p}})\mathrm{e}^{-2\beta d}}{|\,1 - r_{01}^{\mathrm{p}} r_{02}^{\mathrm{p}} \mathrm{e}^{-2\beta d}|^2}$$

Using the relation

$$\mathrm{Im}\left(\frac{\varepsilon - 1}{\varepsilon + 1}\right) = \frac{2\mathrm{Im}(\varepsilon)}{|\,\varepsilon + 1|^2}$$

the spectral heat flux from 1 to 2 in the limit $d \to 0$ can be expressed as

$$q''_{\omega,1-2} \approx \frac{\Theta(\omega, T_1)}{\pi^2 d^2} \frac{\mathrm{Im}(\varepsilon_1)\mathrm{Im}(\varepsilon_2)}{|(\varepsilon_1 + 1)(\varepsilon_2 + 1)|^2} \times \int_{x_0}^{\infty} \left| 1 - \frac{(\varepsilon_1 - 1)(\varepsilon_2 - 1)}{(\varepsilon_1 + 1)(\varepsilon_2 + 1)} \mathrm{e}^{-x} \right|^{-2} x\mathrm{e}^{-x}\,\mathrm{d}x \qquad (23)$$

where $x_0 = 2d\omega/c$. The heat flux will increase with d^{-2} as the distance is reduced. The integral approaches 1 when

$$\left| \frac{(\varepsilon_1 - 1)(\varepsilon_2 - 1)}{(\varepsilon_1 + 1)(\varepsilon_2 + 1)} \right| \ll 1$$

and consequently, the net spectral flux becomes [6,9]

$$q''_{\omega,1-2} - q''_{\omega,2-1} \approx \frac{1}{\pi^2 d^2} \frac{\mathrm{Im}(\varepsilon_1)\mathrm{Im}(\varepsilon_2)}{|(\varepsilon_1 + 1)(\varepsilon_2 + 1)|^2} [\Theta(\omega, T_1) - \Theta(\omega, T_2)] \qquad (23a)$$

When Eq. (23a) is used to calculate the spectral energy flux at $d = 1$ nm for the case shown in Fig. 7b, the predicted values are nearly half of those obtained by integration in the frequency region from 10^{12} rad s^{-1} to 10^{14} rad s^{-1}. Note that Eq. (23) is not applicable for $\omega > 10^{14}$ rad s^{-1}, where the major contribution of evanescent waves is for $\omega/c < \beta < n\omega/c$, i.e., propagating waves in silicon. Therefore, care must be taken in applying Eqs. (23) and (23a) to interpret the behavior of near-field thermal radiation.

The enhanced thermal radiation can also be understood by the very large energy density in the vicinity of the surface. The spectral energy density $u(z, \omega)$ near the surface of medium 1 at 1000 K is evaluated using Eqs. (8) and (10), and the results are shown in Fig. 8 when the medium is either intrinsic silicon or doped silicon with $N_{D1} = 10^{20}\,\mathrm{cm}^{-3}$. The energy density of a blackbody enclosure is also shown for comparison. As the height $z \leqslant 100$ nm, the energy density is greatly enhanced because of the density of states increases rapidly as z decreases towards nanometer regime. Furthermore, the maximum appears at a different wavelength compared to the maximum for Planck's blackbody distribution function. When $\beta \gg \omega/c$, Eq. (10b) reduces to

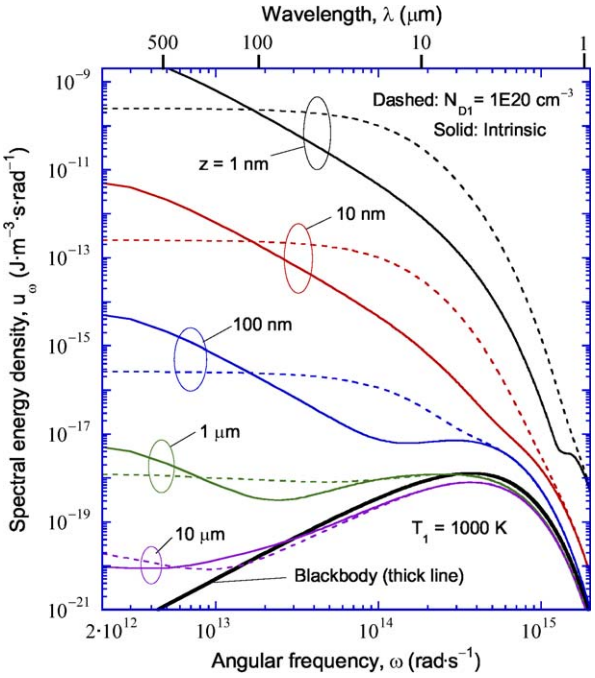

Fig. 8. Spectral energy density near a semi-infinite silicon at $T_1 = 1000$ K at different distances from the surface: (a) intrinsic; (b) dopant concentration $N_{D1} = 10^{20}\,\mathrm{cm}^{-3}$.

$$D_{\mathrm{evan}}(z,\omega) \approx \frac{1}{\pi^2\omega}\frac{\mathrm{Im}(\varepsilon_1)}{|\varepsilon_1+1|^2}\int_{\omega/c}^{\infty} \mathrm{e}^{-2z\beta}\beta^2\,\mathrm{d}\beta$$

By evaluating the integration, one obtains the following asymptotical expression for $z \to 0$, as shown in earlier studies [6,24–26]:

$$D_{\mathrm{evan}}(z,\omega) \approx \frac{1}{4\pi^2\omega z^3}\frac{\mathrm{Im}(\varepsilon_1)}{|\varepsilon_1+1|^2} \tag{24}$$

Eq. (24) suggests that the near-field density of states increases with z^{-3} as z decreases, and is localized at the surface. The dependence of u_ω on doping can be understood by examining the term $\mathrm{Im}(\varepsilon_1)/|\varepsilon_1+1|^2$. Because the plasma frequency of silicon is pushed towards shorter wavelengths by increasing the carrier concentration, $\mathrm{Im}(\varepsilon_1)/|\varepsilon_1+1|^2$ increases significantly in the spectral region from 2 to 100 μm. Although u_ω for intrinsic silicon is larger towards longer wavelengths, the contribution to the total energy density is very small when $\omega < 10^{13}\,\mathrm{rad\,s}^{-1}$. Hence, the near-field energy flux may increase further when the emitter is heavily doped.

Fig. 9 shows the radiation heat transfer between heavily doped silicon. In Fig. 9a, the 1000 K emitter is assumed to have a fixed dopant concentration of $N_{D1} = 10^{20}\,\mathrm{cm}^{-3}$, while the dopant concentration of the 300 K receiver varies from $N_{D2} = 10^{18}$ to $10^{21}\,\mathrm{cm}^{-3}$. The results for $N_{D2} = 10^{20}\,\mathrm{cm}^{-3}$ is slightly lower but very close to that for $N_{D2} = 10^{21}\,\mathrm{cm}^{-3}$ and thus not shown in the figure. As expected, the nanoscale thermal radiation is enormous. For example, at $d = 1$ nm, $q''_{\mathrm{net}} \sim 10^9\,\mathrm{W\,m}^{-2}$ or 15,000 times greater than that between two blackbodies. The effect

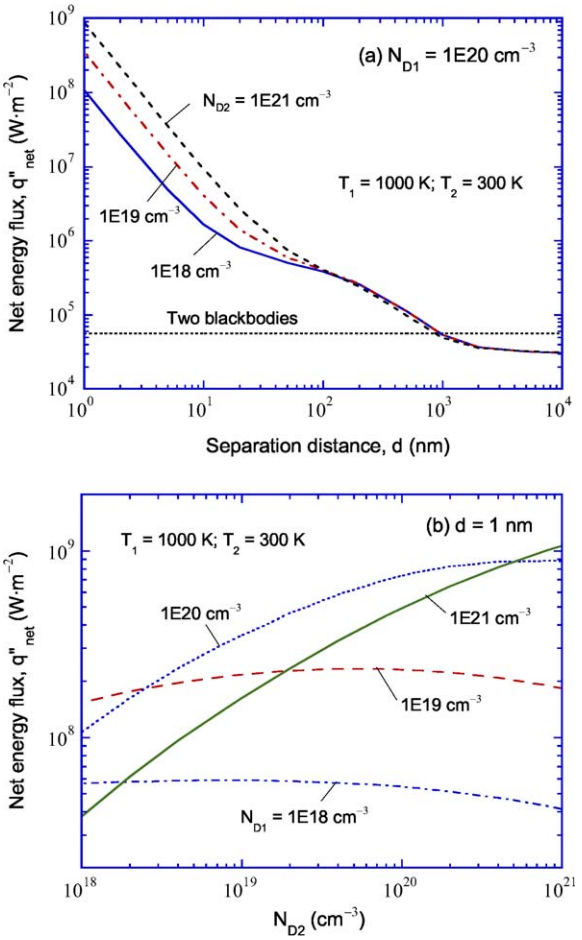

Fig. 9. Effect of doping on the net energy flux between heavily doped silicon at $T_1 = 1000$ K and $T_2 = 300$ K: (a) q''_{net} versus d for several N_{D2} values when $N_{D1} = 10^{20}\,\mathrm{cm}^{-3}$; (b) q''_{net} at $d = 1$ nm versus N_{D2} for different N_{D1} values.

of doping on nanoscale radiation is further demonstrated in Fig. 9b, where the separation distance is fixed at $d = 1$ nm. When $N_{D1} \leqslant 10^{19}\,\mathrm{cm}^{-3}$, the effect of changing N_{D2} is insignificant. However, for $N_{D1} = 10^{20}$ to $10^{21}\,\mathrm{cm}^{-3}$, increasing N_{D2} will result in increasing near-field energy flux. Generally speaking, the enhancement at nanometer scale is proportional to $\frac{\mathrm{Im}(\varepsilon_1)\mathrm{Im}(\varepsilon_2)}{|(\varepsilon_1+1)(\varepsilon_2+1)|^2}$ for given d as discussed earlier.

In the previous examples, the temperatures of medium 1 and medium 2 are set at $T_1 = 1000$ K and $T_2 = 300$ K, respectively, and the net radiation energy flux is calculated for various doping concentrations of silicon. In order to investigate the effect of temperature on the net energy flux, the dopant concentrations of both medium1 and medium 2 are fixed at $N_{D1} = N_{D2} = 10^{20}\,\mathrm{cm}^{-3}$ and the net energy flux is calculated for different values of T_1 when $T_2 = 300$ K. The calculated net energy flux as function of d is presented in Fig. 10a and the ratio of the energy flux from medium 1 to medium 2 to that of blackbody emissive power at T_1 is shown in Fig. 10b. When $T_1 = 400$ K, q''_{net} at 1 nm distance can exceed $1.45 \times 10^8\,\mathrm{W\,m}^{-2}$, which is 146,000 times the net heat flux between two blackbodies placed far apart.

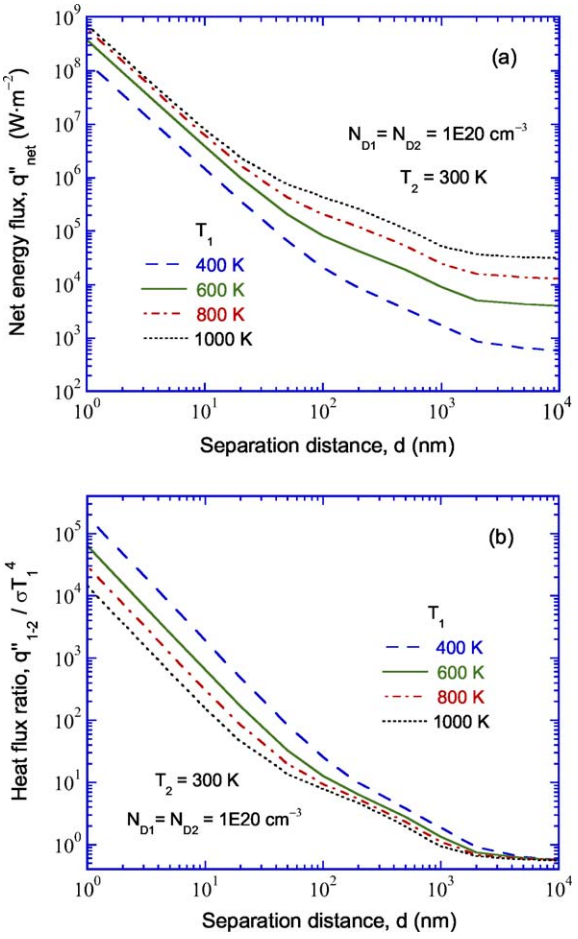

Fig. 10. Effect of source temperature on the radiation energy flux between two doped silicon with $N_{D1} = N_{D2} = 10^{20}$ cm^{-3} and $T_2 = 300$ K: (a) q''_{net} versus d for T_1 from 400 to 1000 K; (b) the energy flux from medium 1 to medium 2 normalized by σT_1^4.

When q''_{1-2} is compared with σT_1^4, as shown in Fig. 10b, the enhancement is greater when T_1 is closer to 300 K and reaches $\approx 2\times10^5$ when $T_1 = 400$ K at $d = 1$ nm. Even at $d = 10$ nm, the enhancement is significant for a number of applications, such as enhanced heating and cooling for thermal control and energy conversion near room temperature.

4.3. Discussion

The enhancement of near-field radiation energy flux obtained from this work is consistent with that obtained by Marquier et al. [22] for heavily doped silicon near room temperature. For SiC, the enhanced near-field radiation has been attributed to surface phonon polaritons [6,13,20,21]. For doped silicon, free-carrier absorption dominates and thus it is helpful to examine the resonance conditions to see whether surface plasmon polaritons can be excited and thus are responsible for the enhancement. A surface polariton is a coupled, localized electromagnetic wave that propagates along the interface of two different media and decay exponentially away from the interface. A necessary requirement for the excitation of surface plasmons at the interface between vacuum and a medium is that Re(ε) must be negative and Im(ε) should be sufficiently small [54]. This can occur with metals (like silver and aluminum) at frequencies lower than the plasma frequency, defined as $\omega_p = N_e e^2/\varepsilon_0 m_e^*$, but much higher than the electron scattering frequency [26]. The resulting Fresnel's reflection coefficient for p-polarization approaches infinity in the lossless case. For doped silicon, the plasma frequency is in the infrared region. Because of the large scattering rate ($1/\tau$), Re(ε) may never be negative; and even in the case when Re(ε) is negative, Im(ε) is too large for surface plasmons to be excited. Therefore, the enhancement of nanoscale radiation may be understood by the large values of the exchange function around the plasma frequency where $\mathrm{Im}(\varepsilon)/|1+\varepsilon|^2$ is large for both media. Although surface plasmon resonance condition is not satisfied, there exist evanescent waves in vacuum as well as in the media for sufficiently large β values. The near-field energy flux spectrum for Si exhibits a broad peak when the doping concentration is less than 10^{18} cm^{-3} as can be seen from Fig. 7. The spectral width of the heat flux peak decreases with increasing doping level but is still much broader than that for SiC.

It is instructive to compare the nanoscale thermal radiation with heat conduction by air since many AFMs are operated in ambient conditions. When d is much smaller than the mean free path, which is about 70 nm at standard atmospheric conditions, boundary scattering or ballistic scattering dominates gas conduction. The thermal conductivity decreases linearly as d decreases, whereas the heat flux is independent of d in this regime. Assuming a thermal accommodation coefficient of 1, the heat transfer by gas conduction can be estimated by [55]

$$q''_{cond} = \frac{c_v(\gamma+1)P}{(8\pi R T_m)^{1/2}}(T_1 - T_2) \tag{25}$$

where R is the ideal gas constant, P is the pressure, $T_m = 4T_1T_2/(\sqrt{T_1}+\sqrt{T_2})^2$ is a mean temperature, and c_v is the specific heat at constant volume evaluated at T_m. The resulting q''_{cond} for air at a pressure $P = 1$ atm is approximately 1.1×10^7 W m^{-2} for $T_1 = 400$ K and $T_2 = 300$ K, and it increases to 6.3×10^7 W m^{-2} when $T_1 = 1000$ K. Therefore, at $d = 1$ nm, near-field radiation heat transfer with heavily doped silicon can be an order of magnitude greater than heat conduction by air at the atmospheric pressure. Because the conduction heat flux further decreases as the pressure is reduced, nanoscale thermal radiation may dominate the heat transfer process for scanning thermal probes and heated cantilever tips using heavily doped silicon.

The radiation heat transfer coefficient can be defined as $h_r = q''_{net}/(T_1 - T_2)$ in analog to Newton's law of cooling. It can be seen from Fig. 10a that for heavily doped silicon $h_r \sim 10^6$ W m^{-2} K^{-1} at $d = 1$ nm and $h_r \sim 10^4$ W m^{-2} K^{-1} at $d = 10$ nm. It is important to estimate whether the local equilibrium assumption is valid. Assuming that the near-field radiation penetration depth is 100 nm and a thermal

conductivity for doped silicon is 100 W m^{-1} K^{-1}, for a heat flux of 10^9 W m^{-2}, the temperature drop would be 1 K within the radiation penetration depth. Therefore, the local equilibrium assumption should still be valid. However, for a wafer of 100 μm thick, the temperature drop would be 1000 K. The above calculations suggest that indeed near-field radiation can be an effective way of heating and cooling. As an alternative to the parallel-plate configuration, it is possible to pattern one of the silicon wafers with a two-dimensional array of truncated cones or pyramids to remove heat locally for thermal control in nanoelectronics, for example.

5. Conclusions

The nanoscale thermal radiation between two closely spaced semi-infinite media is systematically investigated for silicon with varying dopant concentrations and temperatures, under the framework of fluctuational electrodynamics. A Drude model that considers the effects of temperature and dopant concentration on the free carrier concentrations and scattering times is adopted here after a careful parameter selection and comparison with existing optical property data. Enormous enhancement in nanoscale radiation heat transfer has been found for heavily doped silicon. At the separation distance of 1 nm, the net energy flux can exceed 10^9 W m^{-2} with (n-typed) silicon emitter at 1000 K and receiver at 300 K, for dopant concentrations of $N_{D1} = N_{D2} = 10^{21}$ cm^{-3}. The calculated heat flux is 10 times that of air conduction at atmospheric pressure. The radiation heat transfer coefficient can be $h_r \sim 10^6$ W m^{-2} K^{-1} at $d = 1$ nm and $h_r \sim 10^4$ W m^{-2} K^{-1} at $d = 10$ nm. The enhancement of radiation heat transfer at the nanoscale may have an impact on the development of near-field thermal probing and nanomanufacturing techniques. The theoretical understanding gained from the present study will facilitate the design of experiments that utilize near-field heat transfer to enhance heating or cooling at the nanoscale.

Acknowledgements

This work was supported by the National Science Foundation (CTS-0236831 and CTS-0327117) and the Georgia Tech Focused Research Program on Nanoscale Thermal Metrology. Valuable discussions with Professors G. Chen (MIT), J.-J. Greffet (Ecole Central Paris), W.P. King (Georgia Tech), and D.B. Tanner (Univ. Florida) are greatly appreciated. The authors also thank Bong Jae Lee for his assistance in modeling the optical properties of silicon and Keunhan Park for reviewing the manuscript.

References

[1] E.G. Cravalho, C.L. Tien, R.P. Caren, Effect of small spacing on radiative transfer between two dielectrics, J. Heat Transfer 89 (1967) 351–358.

[2] R. Siegel, J.R. Howell, Thermal Radiation Heat Transfer, fourth ed., Taylor and Francis, New York, 2002 (Chapters 3, 7, and 18).

[3] M.F. Modest, Radiative Heat Transfer, McGraw-Hill, New York, 1993 (Chapter 2).

[4] Z.M. Zhang, C.J. Fu, Q.Z. Zhu, Optical and thermal radiative properties of semiconductors related to micro/nanotechnology, Adv. Heat Transfer 37 (2003) 179–296.

[5] J.B. Pendry, Radiative exchange of heat between nanostructures, J. Phys.: Condens. Matter 11 (1999) 6621–6633.

[6] J.-P. Mulet, K. Joulian, R. Carminati, J.-J. Greffet, Enhanced radiative heat transfer at nanometric distances, Microscale Thermophys. Eng. 6 (2002) 209–222.

[7] D. Polder, M. Van Hove, Theory of radiative heat transfer between closely spaced bodies, Phys. Rev. B 4 (1971) 3303–3314.

[8] R.P. Caren, Thermal radiation between closely spaced metal surfaces at low temperatures due to traveling and quasi-stationary components of the radiation field, Int. J. Heat Mass Transfer 17 (1974) 755–765.

[9] J.J. Loomis, H.J. Maris, Theory of heat transfer by evanescent waves, Phys. Rev. B 50 (1994) 18517–18524.

[10] A.I. Volokitin, B.N. Persson, Radiative heat transfer between nanostructures, Phys. Rev. B 63 (2001) 205404/1–205404/11.

[11] J.L. Pan, H.K.H. Choy, C.G. Fonstad Jr., Very large radiative transfer over small distances from a black body for thermophotovoltaic applications, IEEE Trans. Electron Dev. 47 (2000) 241–249.

[12] M.D. Whale, E.G. Cravalho, Modeling and performance of microscale thermophotovoltaic energy conversion devices, IEEE Trans. Energy Conver. 17 (2002) 130–142.

[13] A. Narayanaswamy, G. Chen, Surface modes for near field thermophotovoltaics, Appl. Phys. Lett. 82 (2003) 3544–3546.

[14] C.C. Williams, H.K. Wickramasinghe, Scanning thermal profiler, Appl. Phys. Lett. 49 (1986) 1587–1589.

[15] J.-B. Xu, K. Lauger, R. Moller, K. Dransfeld, I.H. Wilso, Heat transfer between two metallic surfaces at small distances, J. Appl. Phys. 76 (1994) 7209–7216.

[16] W. Müller-Hirsch, A. Kraft, M.T. Hirsch, J. Parisi, A. Kittel, Heat transfer in ultrahigh vacuum scanning thermal microscopy, J. Vac. Sci. Technol. A 17 (1999) 1205–1210.

[17] A. Majumdar, Scanning thermal microscopy, Annu. Rev. Mater. Sci. 29 (1999) 505–585.

[18] Z.M. Zhang, C.J. Fu, Unusual photon tunneling in the presence of a layer with a negative refractive index, Appl. Phys. Lett. 80 (2002) 1097–1099.

[19] C.J. Fu, Z.M. Zhang, D.B. Tanner, Energy transmission by photon tunneling in multilayer structures including negative index materials, J. Heat Transfer 127 (2005) 1046–1052.

[20] J.-P. Mulet, K. Joulian, R. Carminati, J.-J. Greffet, Nanoscale radiative heat transfer between a small particle and a plane surface, Appl. Phys. Lett. 78 (2001) 2931–2933.

[21] A.I. Volokitin, B.N. Persson, Resonant photon tunneling enhancement of the radiative heat transfer, Phys. Rev. B 69 (2004) 045417/1–045417/5.

[22] F. Marquier, K. Joulain, J.-P. Mulet, R. Carminati, J.-J. Greffet, Engineering infrared emission properties of silicon in the near field and the far field, Opt. Commun. 237 (2004) 379–388.

[23] W.P. King, T.W. Kenny, K.E. Goodson, G. Cross, M. Despont, U. Dürig, H. Rothuizen, G.K. Binig, P. Vettiger, Atomic force microscope cantilevers for combined thermomechanical data writing and reading, Appl. Phys. Lett. 78 (2001) 1300–1302.

[24] S.M. Rytov, Yu.A. Krastov, V.I. Tatarskii, Principles of Statistical Radiophysics, vol. 3, Springer-Verlag, New York, 1987 (Chapter 3).

[25] A.V. Shchegrov, K. Joulain, R. Carminati, J.-J. Greffet, Near-field spectral effects due to electromagnetic surface excitations, Phys. Rev. Lett. 85 (2000) 1548–1551.

[26] K. Joulian, R. Carminati, J.-P. Mulet, J.-J. Greffet, Definition and measurement of the local density of states close to an interface, Phys. Rev. B 68 (2003) 245405/1–245405/10.

[27] A.I. Volokitin, B.N.J. Persson, Resonance photon tunneling enhancement of the van der Waals friction, Phys. Rev. Lett. 91 (2003) 106101/1–106101/4.
[28] A.I. Volokitin, B.N.J. Persson, Noncontact friction between nanostructures, Phys. Rev. B 68 (2003) 155420/1–155420/12.
[29] J.R. Zurita-Sanchez, J.-J. Greffet, L. Novotny, Friction forces arising from fluctuating thermal fields, Phys. Rev. A 69 (2004) 022902/1–022902/14.
[30] L. Mandel, E. Wolf, Optical Coherence and Quantum Optics, Cambridge University Press, Cambridge, UK, 1995 (Chapter 6).
[31] K. Joulain, J.-P. Mulet, F. Marquier, R. Carminati, J.-J. Greffet, Surface electromagnetic waves thermally excited: radiative heat transfer, coherence properties and Casimir forces revisited in the near field, Surf. Sci. Rep. 57 (2005) 59–112.
[32] J.E. Sipe, New Green-function formalism for surface optics, J. Opt. Soc. Am. B 4 (1987) 481–489.
[33] P.J. Timans, The thermal radiative properties of semiconductors, in: F. Roozeboom (Ed.), Advances in Rapid Thermal and Integrated Processing, Kluwer Academic Publishers, The Netherlands, 1996, pp. 35–101.
[34] S.M. Sze, Physics of Semiconductor Devices, John Wiley & Sons, New York, 1981 (Chapter 1).
[35] W.G. Spitzer, H.Y. Fan, Determination of optical constants and carrier effective mass of semiconductors, Phys. Rev. 106 (1957) 882–890.
[36] P.J. Hesketh, J.N. Zemel, B. Gebhart, Polarized spectral emittance from periodic micromachined surfaces. II. Doped silicon: angular variation, Phys. Rev. B 37 (1988) 10803–10813.
[37] M. Auslender, S. Hava, Zero infrared reflectance anomaly in doped silicon lamellar gratings. I. From antireflection to total absorption, Infrared Phys. Technol. 36 (1995) 1077–1088.
[38] J.P. Hebb, Pattern effects in rapid thermal processing, Ph.D. Dissertation, Department of Mechanical Engineering, Massachusetts Institute of Technology, Cambridge, MA, 1997.
[39] H.H. Li, Refractive index of silicon and germanium and its wavelength and temperature derivatives, J. Phys. Chem. Ref. Data 9 (1980) 561–658.
[40] B.J. Lee, Z.M. Zhang, E.A. Early, D.P. DeWitt, B.K. Tsai, Modeling radiative properties of silicon with coatings and comparison with reflectance measurements, J. Thermophys. Heat Transfer 19 (2005) 558–569.
[41] P.J. Timans, Emissivity of silicon at elevated temperature, J. Appl. Phys. 74 (1993) 6353–6364.
[42] G.G. MacFarlane, T.P. McLean, J.E. Quarrington, V. Roberts, Fine structure in the absorption-edge spectrum of Si, Phys. Rev. 111 (1958) 1245–1254.
[43] D.F. Edwards, Silicon (Si), in: E.D. Palik (Ed.), Handbook of Optical Constants of Solids, vol. 1, Academic Press, New York, 1998, pp. 547–570.
[44] W.E. Beadle, J.C.C. Tsai, R.D. Plummer, Quick Reference Manual for Silicon Integrated Circuit Technology, John Wiley & Sons, New York, 1985 (Chapters 1 and 2).
[45] F.J. Morin, J.P. Maita, Electrical properties of silicon containing arsenic and boron, Phys. Rev. 96 (1954) 28–35.
[46] P. Vandenabeele, K. Maex, Influence of temperature and backside roughness on the emissivity of Si wafers during rapid thermal processing, J. Appl. Phys. 72 (1992) 5867–5875.
[47] H. Rogne, P.J. Timans, H. Ahmed, Infrared absorption in silicon at elevated temperatures, Appl. Phys. Lett. 69 (1996) 2190–2193.
[48] J.C. Sturm, C.M. Reaves, Silicon temperature measurement by infrared absorption: fundamental processes and doping effects, IEEE Trans. Electron Dev. 39 (1992) 81–88.
[49] C.D. Thurmond, The standard thermodynamic functions for the formation of electrons and holes in Ge, Si, GaAs, and GaP, J. Electrochem. Soc.: Solid State Sci. Technol. 122 (1975) 1133–1141.
[50] S.M. Sze, Semiconductor Devices: Physics and Technology, second ed., John Wiley & Sons, New York, 2002 (Chapter 2).
[51] T.K. Gaylord, J.N. Linxwiler Jr., A method for calculating the Fermi energy and carrier concentrations in semiconductors, Am. J. Phys. 44 (1976) 353–356.
[52] I.W. Boyd, T.D. Binnie, J.I.B. Wilson, M.J. Colles, Absorption of infrared radiation in silicon, J. Appl. Phys. 55 (1984) 3061–3063.
[53] P.A. Schumann Jr., W.A. Keenan, A.H. Tong, H.H. Gegenwarth, C.P. Schneider, Silicon optical constants in the infrared, J. Electrochem. Soc.: Solid State Sci. 118 (1971) 145–148.
[54] H. Raether, Surface Plasmons on Smooth and Rough Surfaces and on Gratings, Springer-Verlag, Berlin, 1988 (Chapter 2).
[55] E.H. Kennard, Kinetic Theory of Gases, McGraw-Hill, New York, 1938.